

Gd³⁺-Functionalized Lithium Niobate Nanoparticles for Dual Multiphoton and Magnetic Resonance Bioimaging

Raphaël De Matos, Adrian Gheata, Gabriel Campargue, Jérémy Vuilleumier, Laura Nicolle, Katarzyna Pierzchala, Ileana Jelescu, Fiorella Lucarini, Ivan Gautschi, Florian Riporto, Ronan Le Dantec, Yannick Mugnier, Anne-Sophie Chauvin, Marinella Mazzanti, Davide Staedler, Dario Diviani, Luigi Bonacina, and Sandrine Gerber-Lemaire*



Cite This: *ACS Appl. Nano Mater.* 2022, 5, 2912–2922



Read Online

ACCESS |



Metrics & More



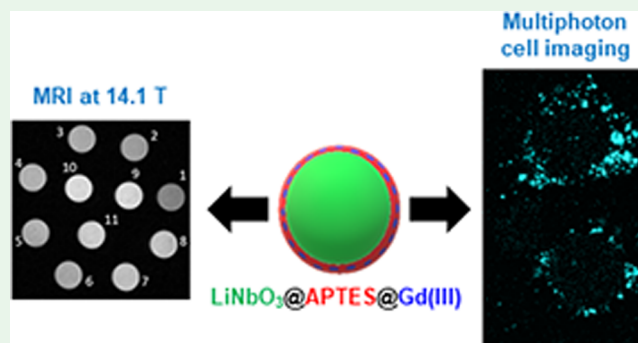
Article Recommendations



Supporting Information

ABSTRACT: Harmonic nanoparticles (HNPs) have emerged as appealing exogenous probes for optical bioimaging due to their distinctive features such as long-term photostability and spectral flexibility, allowing multiphoton excitation in the classical (NIR-I) and extended near-infrared spectral windows (NIR-II and -III). However, like all other optical labels, HNPs are not suitable for whole-body imaging applications. In this work, we developed a bimodal nonlinear optical/magnetic resonance imaging (MRI) contrast agent through the covalent conjugation of Gd(III) chelates to coated lithium niobate HNPs. We show that the resulting nanoconjugates exert strong contrast both in T_1 -weighted MRI of agarose gel-based phantoms and in cancer cells by harmonic generation upon excitation in the NIR region. Their capabilities for dual T_1/T_2 MRI were also emphasized by the quantitative mapping of the phantom in both modes. The functionalization protocol ensured high stability of the Gd-functionalized HNPs in a physiological environment and provided a high r_1 relaxivity value per NP ($5.20 \times 10^5 \text{ mM}^{-1} \text{ s}^{-1}$) while preserving their efficient nonlinear optical response.

KEYWORDS: dual imaging modality, multiphoton microscopy, MRI T_1 contrast agents, surface functionalization, harmonic generation, dielectric nanoparticles



INTRODUCTION

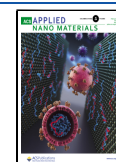
Cellular¹ and immunocellular therapies² are rightfully listed among the most promising biomedical approaches for the years to come. The translation of these techniques to clinical practice requires the careful assessment of the fate of a selected cell population in the host organism. Tracking these cells individually poses several challenges in terms of sensitivity, selectivity, spatial resolution, penetration depth, and monitoring time span.³ While the use of exogenous probes can greatly improve sensitivity and contrast⁴ in comparison to the signal from endogenous structures, none of the available imaging techniques can simultaneously provide (sub)cellular spatial resolution and whole-body imaging capabilities and hence the idea pursued by several research groups to develop dual agents capable of exerting contrast by different physical mechanisms. The range of techniques that can be exploited include magnetic resonance imaging (MRI), computed tomography (CT), ultrasound, photoacoustic imaging, luminescence imaging, and linear and nonlinear microscopy.⁵ MRI has virtually no limitation in terms of penetration depth, and it does not involve ionizing radiation. On the downside, its

spatial resolution in the order of tens of micrometers greatly exceeds the cell dimensions. On the opposite end of the spectrum, confocal optical microscopy provides submicron resolution in the three dimensions but considerably poorer sample penetration (hundreds of micrometers). Multiphoton microscopy stands as an interesting alternative as the longer wavelengths used for excitation suffer less from tissue scattering. Recently, thanks to the advent of new laser sources covering the second and third near-infrared windows⁶ [NIR-II and -III, alternatively referred to as the short-wave infrared region (SWIR)], penetration depths of the order of a millimeter have been reported.⁷ One drawback associated with the use of SWIR excitation is related to the limited number of optical probes responding in this spectral region.^{8,9}

Received: January 10, 2022

Accepted: January 25, 2022

Published: February 3, 2022



Multifunctional nanoparticles (NPs) attracted a growing interest over the past decade for the development of multimodal probes for both *in vitro* and *in vivo* bioimaging and theranostic applications.^{10–17} Owing to high agent loading ability and their surface properties which allow for tailored chemical modifications, inorganic NPs emerged as excellent candidates for engineering multimodal probes. Seminal achievements were reported with lanthanide-doped upconversion NPs for the combination of NIR luminescence imaging with complementary MRI, X-ray CT, or positron emission tomography (PET) imaging modalities.^{18–22} Nanoconjugates based on iron oxide NPs were also disclosed for dual MRI/PET and MRI/CT tumor imaging.^{23,24} Due to their ultrasmall size and luminescence properties, noble-metal nanoclusters were conjugated to gadolinium (Gd) ions to provide hybrid nanoprobe for targeted triple-modal NIR fluorescence/MRI/CT *in vivo* tumor imaging.^{25,26} In addition to their multimodal imaging capabilities, nanoparticulate systems were used to increase the local concentration and efficiency of Gd-based MRI contrast agents by providing an effective delivery of reporters and a high payload of paramagnetic ions to the target sites.^{27–31} Recently, harmonic NPs (HNPs) were proposed as highly efficient NIR probes presenting several complementary advantages with respect to other optically active NPs,^{32–34} including the flexibility of the excitation wavelength, the absence of saturation, bleaching/blinking events,³⁵ and the possibility of colocalizing the simultaneously emitted second and third harmonic signals excited for their identification in optically complex environments such as tumor tissues.³⁶ We previously demonstrated the potential of bismuth ferrite (BiFeO₃) HNPs for cell labeling and tracking by NIR-II multiphoton microscopy in both muscle and lung tissues.^{37,38} Sugiyama et al. reported the labeling of hematopoietic stem cells with low concentrations of barium titanate (BaTiO₃) HNPs to understand their cellular uptake and intracellular fate,³⁹ and other authors demonstrated their *in vivo* application.^{40,41} The inherent flexibility and stability of the nonlinear response of HNPs upon excitation from UV to NIR-II,³³ NIR-III,⁴² and NIR-IV⁴² would be highly advantageous in the context of multimodal imaging combining their capability for nonlinear optical response with magnetic properties for MRI. Recently, the surface decoration of BaTiO₃ HNPs with gold or silver NPs allowed for combined two-photon second harmonic generation (SHG) imaging and one-photon surface-enhanced Raman scattering in living cells.⁴³

Herein, we disclose the first nanoconjugate based on a lithium niobate (LiNbO₃, LNO) harmonic core⁴⁴ functionalized with chelated Gd³⁺ ions for bimodal optical/MR bioimaging. The conjugation strategy made use of copper-catalyzed [3 + 2] cycloaddition (click reaction) at the surface of silica-coated LNO HNPs with a terminal alkyne-modified analogue of the tripodal propionate ligand H₃ebpatcn.⁴⁵ First, we assessed the nonlinear optical imaging properties of the resulting Gd³⁺-functionalized LNO HNPs upon incubation with DU145 human prostate cancer cells. Successively, we studied the longitudinal and transverse relaxation rates of water protons in the presence of these nanoconjugates at 30 and 60 MHz, followed by the calculation of their proton relaxivities. Further investigation of their ability to be used as dual T₁–T₂ contrast agents included single phantom experiments using a 9.4 T NMR spectrometer and 14.1 T MRI quantitative T₁ and T₂ mapping, which demonstrated the capability of Gd-

conjugated LNO HNPs to act as bimodal MRI contrast agents and efficient optical markers for multiharmonic imaging.

EXPERIMENTAL SECTION

Electron Microscopy. High-angle annular dark field–scanning transmission electron microscopy (HAADF-STEM) images were acquired on a FEI Tecnai Osiris at 200 kV using the following parameters: probe 0.8 nA, collection angle 10 mrad, CL 115 mm. Energy-dispersive X-ray (EDX) spectroscopy elemental maps were acquired on a FEI Tecnai Osiris using a super-X detector. The samples were prepared by drop-casting a colloidal suspension of LNO-Gd NPs on thin amorphous carbon films (Electron Microscopy Sciences).

X-ray Photoelectron Spectroscopy Analysis. Measurements were carried out on a Phi VersaProbe II (Physical Electronics Inc., MN, USA) using the monochromated K α X-ray line of an aluminum anode (1486.6 eV) operated at ~50 W. The X-ray photoelectron spectroscopy (XPS) spectrum acquisition was performed according to the parameters previously described.⁴⁶ Details on the calculation of surface atomic concentrations are given in the [Supporting Information](#) (S-20), Table S1.

Cell Imaging. 150,000 DU145 human prostate cancer cells were seeded in 29 mm glass-bottom dishes (Cellvis, D29-20-1.5-N) using the RPMI 1640 medium supplemented with GlutaMAXTM (GIBCO N° 61870036), nonessential amino acids (GIBCO N° 1140035), 10% heat-inactivated fetal bovine serum (FBS) (GIBCO N° 10270106), and gentamycin (100 μ g/mL) (GIBCO N° 15750045). The cell layers were then washed once with phosphate-buffered saline (PBS) and treated with LNO-Gd NPs (50 μ g/mL) in the medium. After 48 h of incubation, the cell layers were washed twice with PBS, fixed for 20 min using 4% paraformaldehyde (PFA), and finally stained with DAPI (Roth, 6335.1) (1:5000) for 30 min.

A Leica SP8 Dive Falcon upright multiphoton microscope coupled with an Insight X3 tunable femtosecond laser (Newport Spectra-Physics) was used to acquire the multiphoton images of the fixed cells. The laser was focused onto the sample by a Leica HC FLUOTAR L 25 \times /0.95 water-immersion objective. The epi-collected signals were separated within tailored spectral ranges using the Leica 4Tune system and detected by a photomultiplier and a hybrid detector. We proceeded by simultaneously acquiring the third harmonic generation (THG) and SHG channels upon excitation at 1250 nm first and successively the SHG and DAPI channels upon 800 nm excitation.

Relaxation Measurements. The analyses were performed on permanent magnets (Bruker Minispec spectrometers) with the proton frequencies at 30 MHz (0.7 T) and 60 MHz (1.4 T). LNO, LNO-N₃, or LNO-Gd NPs were suspended in H₂O (600 μ L, 2 mg/mL) in 5 mm NMR tubes and ultrasonicated for 30 min. Complex **8** was dissolved in H₂O (600 μ L, 1.36 mM) in a 5 mm NMR tube. The samples were loaded in the spectrometer, and the temperature was stabilized at 37 °C for 15 min. The longitudinal relaxation time (T₁) was measured with the inversion recovery method, and the transverse relaxation time (T₂) was measured with the Carr–Purcell–Meiboom–Gill (CPMG) spin echo sequence. All measurements correspond to an average over 4 scans. The acquisition parameters were adapted from ref 46 and are given in the [Supporting Information](#) (S-21).

The relaxation rate R_i (s^{−1}) was calculated using eq 1

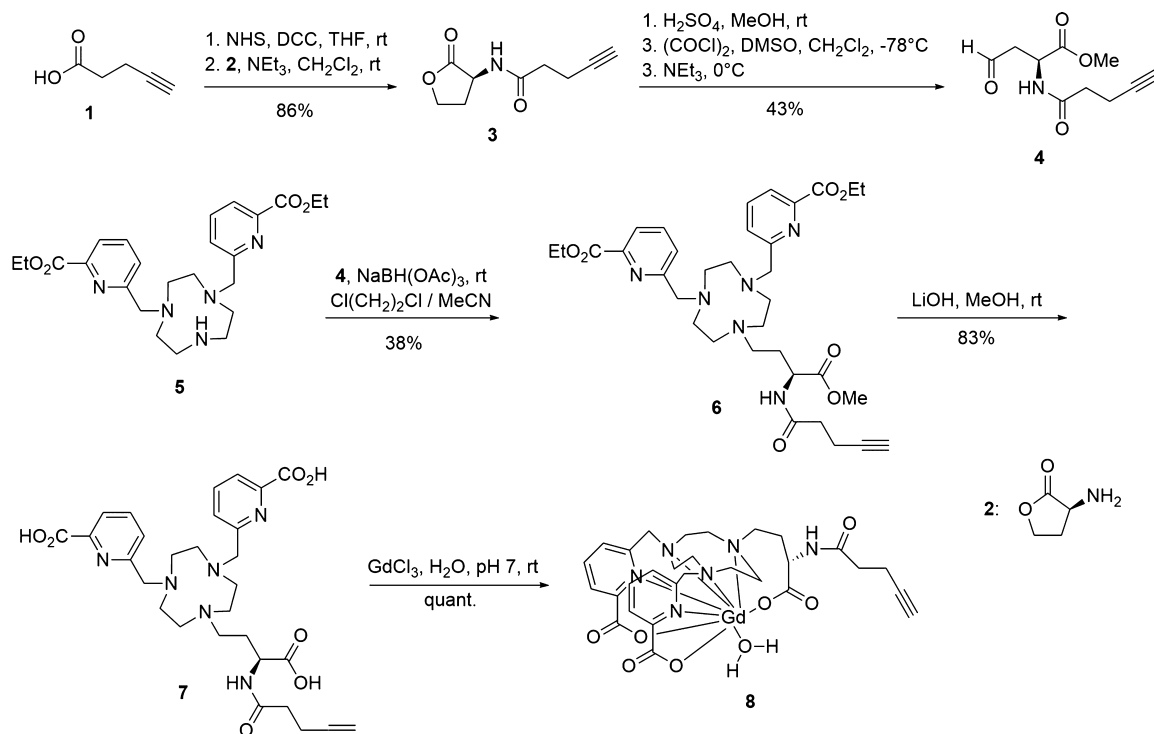
$$R_i = \frac{1}{T_i} \quad (1)$$

The relaxivity values (mM^{−1} s^{−1}) were calculated using eq 2

$$r_i = \frac{\frac{1}{T_i} - \frac{1}{T_{id}}}{c} \quad (2)$$

(where $i = 1$ is the longitudinal relaxation, $i = 2$ is the transverse relaxation of water in the presence of the paramagnetic relaxing agent, and c = concentration of paramagnetic species [mM]). T_{id} stands for the longitudinal or transverse relaxation of pure deionized water

Scheme 1. Synthesis of the TACN-Gd Derivative 8 to Be Conjugated to the LNO HNPs

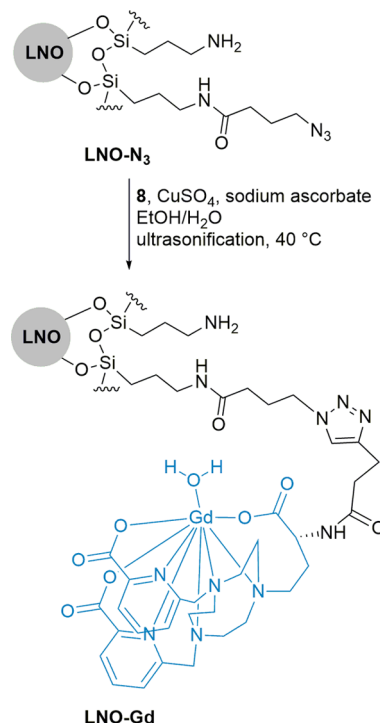


protons. The concentration of Gd(III) ions was determined by ICP-MS analysis (NexIon 350D, PerkinElmer). The T_1 , R_2 , and r_1 values are detailed in the Supporting Information (S-21 and S-22).

Agarose Phantom Relaxation Measurements and MRI. The LNO-Gd NPs (suspended in water, 2 mg/mL) were mixed with a transparent solution of agarose (1.5%) in PBS (pH = 7.4, 144 mg/L KH_2PO_4 , 9000 mg/L NaCl, 795 mg/L $\text{Na}_2\text{HPO}_4 \cdot 7\text{H}_2\text{O}$) at 10 different concentrations: 1.50, 1.25, 1.00, 0.75, 0.50, 0.25, 0.20, 0.15, 0.10, and 0.00 mg/mL, and they were transferred into 5 mm NMR tubes. The T_1 and T_2 relaxation constants were measured at 37 °C and 9.4 T (400 MHz for ^1H) on a Bruker spectrometer equipped with an AVNeo console and 5 mm BBI probe using saturation recovery and CPMG sequences. To avoid relaxation damping during saturation due to high ^1H concentration, the probe was slightly detuned. The variable T_1 relaxation delays were set to 0.001, 0.010, 0.050, 0.075, 0.100, 0.250, 0.500, 0.750, 2.5, 5, 10, and 25 s. The relaxation times T_1 were extracted, fitting the data with a monoexponential build-up. The T_2 echo delay was set to 2 ms, and the variable CPMG loop counters were set to 2, 4, 6, 8, 10, 12, 16, 24, 32, 48, 64, and 128. The relaxation times T_2 were extracted, fitting the data with a monoexponential decay. For MRI, the NMR tubes were then inserted into the homemade Teflon NMR tube holder phantom. The MRI experiments were performed on a 14.1 T Bruker AVANCE Neo system using ParaVision 360 software (Bruker BioSpin, D). A RAPID Biomedical GmbH volume coil was used for transmission and reception. 2D T_1 - and T_2 -weighted contrast images were collected using a gradient-echo sequence/fast low-angle shot (FLASH) with the following parameters: T_1 -TE/TR = 2.75/500 ms, flip angle = 45°, T_2 -TE/TR = 12/5000 ms, flip angle = 136.42°, matrix size = 186 × 186, FOV = 27.9 × 27.9 mm², 9 axial 1 mm slices, 1 average. The repetition time (TR) was chosen to yield good contrast between the different samples at 14.1 T based on the T_1 and T_2 relaxation time range measured at 9.4 T.

Synthesis Protocols. The designation of the compounds refers to the chemical structures presented in Schemes 1 and 2. Chemicals (Aldrich, Acros, Fluka, Sigma, Maybridge, TCI Chemicals, Apollo, abcr, and Fluorochem) and reagent-grade solvents (Fluka, Riedel-de-Haën) were used without further purification. All reactions were performed in flame-dried glassware under an inert atmosphere.

Scheme 2. Conjugation of the Gd(III) Complex to the Surface of Silanized LNO HNPs through Copper-Catalyzed [3 + 2] Cycloaddition



Completion of the reactions was monitored by thin-layer chromatography (TLC) on precoated aluminum plates. Purifications were performed by flash column chromatography (FCC) on silica gel (Merck N° 9385 silica gel 60, 230–400 mesh, particle size 40–63 μm) or by dialysis against water at rt using dialysis tubes of X12 Float-A-Lyzer G2 CE (10 mL, exclusion limit 100–500 Da). Lyophilizations were performed in a VaCo 5 freeze dryer (Zirbus, 0.3 mbar, −80

°C). NMR and IR analyses, as well as accurate mass determination, were performed according to the operating protocols previously described.⁴⁷

Preparation of Compound 3. A solution of pent-4-ynoic acid (3.00 g, 30.58 mmol, 1.0 equiv) and *N*-hydroxysuccinimide (3.52 g, 30.58 mmol, 1.0 equiv) in dry THF (100 mL) was cooled to 0 °C. *N,N'*-dicyclohexylcarbodiimide (6.31 g, 30.58 mmol, 1.0 equiv) dissolved in dry THF (35 mL) was added dropwise, and the mixture was stirred at 0 °C for 45 min. The mixture was warmed to rt and stirred for 2 h. The mixture was filtered and concentrated under reduced pressure. The residue was dissolved in EtOAc (100 mL) and filtered to discard the nonsoluble residues. The filtrate was washed with a saturated aqueous solution of NaHCO₃ (100 mL) and brine (100 mL), dried over MgSO₄, filtered, and concentrated under reduced pressure to afford 2,5-dioxopyrrolidin-1-yl pent-4-ynoate as a white solid (28.7 mmol, 5.60 g). This intermediate (3.00 g, 15.2 mmol, 1.0 equiv) was added dropwise to a solution of (*S*)-(-)- α -amino- γ -butyrolactone hydrobromide (**2**, 3.04 g, 16.72 mmol, 1.1 equiv) and NEt₃ (6.3 mL, 45.6 mmol, 3.0 equiv) in dry DCM (130 mL). The solution was stirred at rt for 2 h. The reaction mixture was washed with a saturated aqueous solution of NH₄Cl (100 mL). The aqueous layer was extracted with DCM (100 mL, eight times). The combined organic layers were dried over MgSO₄, filtered, and concentrated under reduced pressure. The crude product was purified by FCC (PE/EtOAc 1:3) to afford **3** as a white solid (2.56 g, 14.0 mmol, 86% over two steps). The NMR data were in accordance with the previously reported structures.⁴⁶ ¹H NMR spectrum (Supporting Information S-8).

Preparation of Compound 4. To a solution of **3** (500 mg, 2.76 mmol, 1.0 equiv) in MeOH (3 mL) was added concentrated H₂SO₄ (cat., 5 drops), and the mixture was stirred at rt for 24 h. The mixture was cooled to 0 °C, and the reaction was neutralized by the addition of NaHCO₃ (until pH 7). The mixture was filtered and concentrated under reduced pressure at rt to afford methyl pent-4-ynoyl-*L*-homoserinate (600 mg, 2.76 mmol), which was used in the oxidation step without further purification. A solution of (COCl)₂ (0.24 mL, 2.76 mmol, 2.0 equiv) in dry DCM (8 mL) was cooled to -78 °C. DMSO (0.39 mL, 5.52 mmol, 4.0 equiv) in dry DCM (4 mL) was added dropwise, and the mixture was stirred at -78 °C for 10 min. Methyl pent-4-ynoyl-*L*-homoserinate (294 mg, 1.38 mmol, 1.0 equiv) in dry DCM (4 mL) was added dropwise, and the mixture was stirred at -78 °C for 30 min. Et₃N (1.15 mL, 8.28 mmol, 6.0 equiv) was added dropwise, and the mixture was warmed to 0 °C and stirred for 2 h. H₂O (10 mL) was added, and the aqueous layer was extracted with DCM (10 mL, 8 times). The combined organic layers were dried over MgSO₄, filtered, and concentrated under reduced pressure. The crude product was purified by FCC (PE/EtOAc 1:3) to afford **4** as a yellow oil (126 mg, 0.60 mmol, 43%). ¹H NMR (400 MHz, chloroform-*d*): δ 9.71 (s, 1H), 6.56 (d, *J* = 7.7 Hz, 1H), 4.87 (dt, *J* = 7.8, 4.6 Hz, 1H), 3.75 (s, 3H), 3.17 (ddd, *J* = 18.7, 4.8, 0.7 Hz, 1H), 3.12–3.04 (m, 1H), 2.56–2.38 (m, 4H), 1.99 (t, *J* = 2.5 Hz, 1H). ¹³C NMR (101 MHz, chloroform-*d*): δ 199.5, 171.2, 170.9, 82.7, 69.7, 53.0, 47.4, 45.7, 35.2, 14.9. HRMS (ESI/QTOF): *m/z* calcd for C₁₀H₁₄NO₄⁺, ([*M* + *H*]⁺): 212.0917; found, 212.0921. ¹H NMR, ¹³C NMR spectra, IR data (Supporting Information S-8).

Preparation of Compound 6. To a solution of **5** (50 mg, 0.11 mmol, 1.0 equiv) in 1,2-dichloroethane (DCE)/acetonitrile dry (2:1, 0.6 mL), the *L*-homoserine derivative **4** (47 mg, 0.22 mmol, 2.0 equiv) in DCE/MeCN (2:1, 0.6 mL) was added dropwise, followed by NaBH₃CN (35 mg, 0.55 mmol, 5.0 equiv), and the mixture was stirred at rt for 16 h. A saturated aqueous solution of NaHCO₃ (5 mL) was added, and the aqueous layer was extracted with DCM (2 mL, 8 times). The combined organic layers were dried over MgSO₄, filtered, and concentrated under reduced pressure. The crude product was purified by FCC [Al₂O₃ basic III (4.9% water) DCM/MeOH 1:0 and then 50:1] to afford the product as a yellow oil (27 mg, 0.05 mmol, 38%). ¹H NMR (400 MHz, acetonitrile-*d*₃): δ 7.93 (dd, *J* = 7.6, 1.2 Hz, 2H), 7.86 (t, *J* = 7.7 Hz, 2H), 7.73 (d, *J* = 7.7 Hz, 2H), 7.20 (s, 1H), 4.49 (td, *J* = 8.0, 4.6 Hz, 1H), 4.36 (q, *J* = 7.1 Hz, 4H), 3.86 (s, 4H), 3.64 (s, 3H), 2.93–2.71 (m, 12H), 2.60–2.51 (m, 2H),

2.46–2.32 (m, 4H), 2.19–2.15 (m, 2H), 1.82–1.78 (m, 1H), 1.36 (t, *J* = 7.1 Hz, 6H). ¹³C NMR (101 MHz, acetonitrile-*d*₃): δ 174.1, 171.8, 166.2, 148.6, 138.4, 127.5, 126.4, 124.2, 84.3, 70.1, 65.2, 62.3, 56.4, 54.5, 52.6, 52.0, 35.3, 26.3, 15.1, 14.6. HRMS (nanochip-ESI/LTQ-Orbitrap): *m/z* calcd for C₃₄H₄₇N₆O₇⁺, ([*M* + *H*]⁺): 651.3501; found, 651.3510. ¹H NMR, ¹³C NMR spectra, IR data (Supporting Information S-10).

Preparation of Compound 7. To a solution of **6** (10 mg, 15 μ mol, 1.0 equiv) in MeOH/H₂O (5:1, 1.0 mL), LiOH (1.2 mg, 50 μ mol, 3.3 equiv) was added, and the mixture was stirred at rt for 3 h. The reaction mixture was diluted with H₂O (2 mL) and washed with DCM (2 mL). The aqueous phase was then neutralized with HCl 1 M. The resulting solution was transferred to a dialysis tube (MWCO 0.5 kDa) and dialyzed against water for 3 days. Lyophilization afforded **7** as a yellow solid (7.5 mg, 12 μ mol, 83%). ¹H NMR (400 MHz, water-*d*₂): δ 7.85 (t, *J* = 7.80 Hz, 2H), 7.69 (m, 2H), 7.35 (m, 2H), 4.46 (s, 4H), 4.13 (dd, *J* = 7.9, 5.0 Hz, 1H), 3.68 (m, 12H), 3.37 (ddd, *J* = 30.4, 12.0, 4.9 Hz, 2H), 2.48 (m, 6H), 2.27 (s, 1H). ¹³C NMR (100 MHz, water-*d*₂): δ 174.86, 174.10, 170.05, 151.16, 139.72, 125.51, 123.84, 70.01, 59.42, 54.62, 50–52, 34.23, 26.77, 14.36. HRMS (nanochip-ESI/LTQ-Orbitrap): *m/z* calcd for C₂₉H₃₈N₆O₇⁺, ([*M* + *H*]⁺): 582.2796; found, 582.2791. ¹H NMR, ¹³C NMR spectra (Supporting Information S-11).

Preparation of Gd Chelate 8. To a solution of **7** (10 mg, 16 μ mol, 1.0 equiv) in H₂O (500 μ L) was added GdCl₃·6 H₂O (6.3 mg, 17 μ mol, 1.1 equiv), and the mixture was stirred at 37 °C for 16 h. The pH of the reaction mixture was maintained at 7.0 by the addition of an aqueous solution of NH₄OH (0.1 M). The resulting solution was transferred to a dialysis tube (MWCO 0.5 kDa) and dialyzed against water for 3 days. Lyophilization afforded **8** as a yellow solid (13 mg, 16 μ mol, quant.). HRMS (ESI/QTOF): *m/z* calcd for C₂₉H₃₃GdN₆NaO₇⁺, ([*M* + *Na*]⁺): 758.1544; found, 758.1549.

Preparation of LNO-Gd NPs. The surface functionalization protocol for the conjugation of **8** to LNO-N₃ NPs was adapted from ref 47 using copper-catalyzed [3 + 2] cycloaddition with the following quantities: LNO-N₃ NPs (2 mg), **8** (0.76 mg, 1 μ mol, 1.0 equiv), copper (II) sulfate (0.5 equiv, 0.5 μ mol, 80 μ g), and sodium ascorbate (1.5 equiv, 1.5 μ mol, 0.3 mg) in a mixture of EtOH/H₂O (1 mL:1.5 mL). The resulting LNO-Gd NPs were stored in distilled water (2 mg/mL) at 4 °C.

RESULTS AND DISCUSSION

Synthesis of the Chelating Ligand and Gd(III) Complexation. Tripodal picolinate ligands based on a 1,4,7-triazacyclononane (TACN) core were reported as efficient chelators for Gd(III) ions, leading to favorable relaxivity for MRI applications^{45,48} and remarkable contrast efficiency in nanosized formulations.^{27,28} The design of the chelating unit to be conjugated to the surface of HNPs made use of the previously reported disubstituted TACN derivative **5**⁴⁵ (synthesis protocols detailed in the Supporting Information, S-3) for Gd(III) coordination (Scheme 1). The *L*-homoserine analogue **4** was synthesized from (*S*)-(-)- α -amino- γ -butyrolactone (**2**) by coupling with pentynoic acid, followed by nucleophilic ring opening and the subsequent Swern oxidation of the resulting highly sensitive primary alcohol. Reductive amination on the secondary amine of the TACN core delivered the protected chelating ligand **6**, presenting eight coordination moieties and a terminal alkyne for the click reaction at the surface of the HNPs. Saponification in the presence of LiOH followed by dialysis against water delivered the Gd(III) chelator **7** in good yield. A subsequent reaction with GdCl₃ led to the Gd(III)-containing complex **8** for further conjugation to the imaged NPs.

Coating and Functionalization of the LNO HNPs. The surface modification of LNO HNPs (prepared by a non-aqueous solvothermal route from alkoxides;⁴⁴ for TEM images,

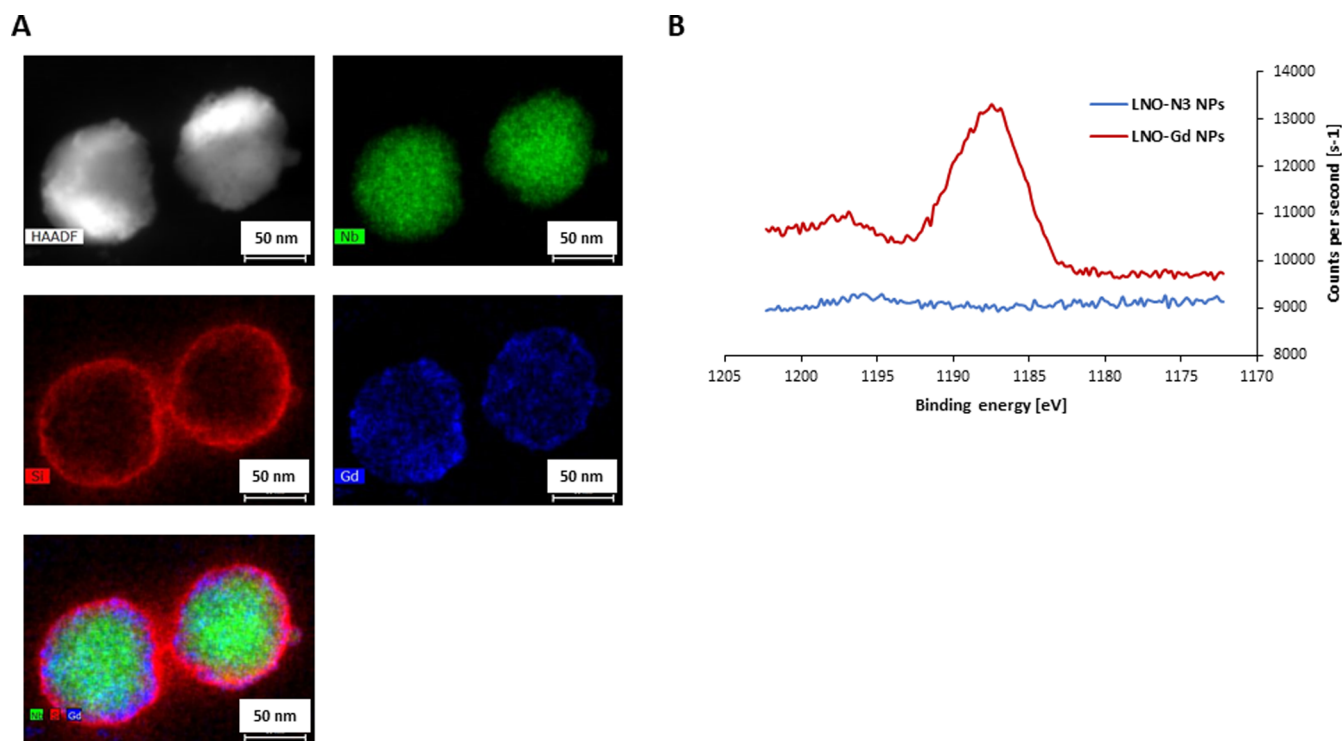


Figure 1. Characterization of LNO-Gd NPs. (A) Representative STEM images. Upper row: HAADF-STEM image, Nb EDX map; middle row: Si EDX map, Gd EDX map; lower row: Nb, Si and Gd EDX maps; scale bar: 50 nm. (B) XPS measurements. Multiplexes of the Gd3d peak from LNO-N₃ NPs (blue) and LNO-Gd NPs (red).

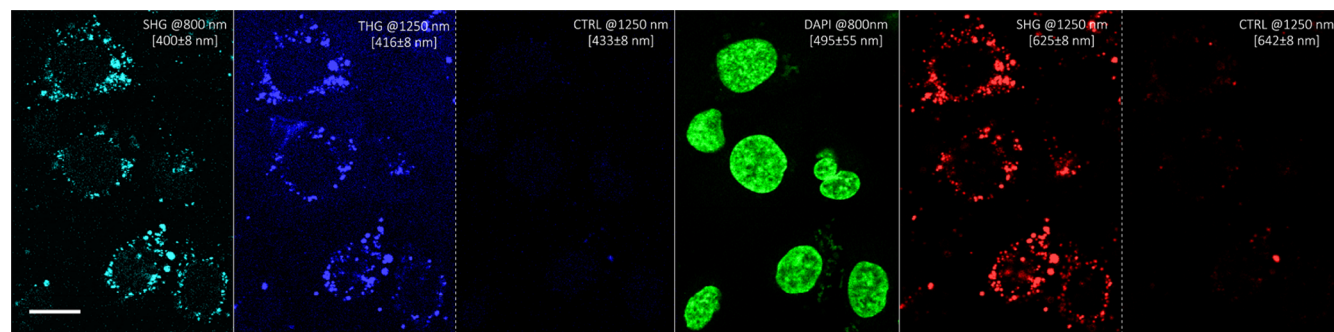


Figure 2. Set of multiphoton images obtained on DU145 human prostate cancer treated with LNO-Gd NPs at 50 µg/mL. In each panel, the labels indicate the signal attribution (THG, SHG, ...), the excitation wavelength (800 or 1250 nm), and the spectral range for channel acquisition. Panels labeled CTRL are the control images acquired and plotted using the same settings of the corresponding THG and SHG images excited at 1250 nm to highlight the narrow bandwidth of the harmonic emission. Scale bar: 20 µm.

see the [Supporting Information](#), Figure S1) followed the coating procedure established by our group for the surface silanization of metal oxide HNPs.⁴⁷ A suspension of azido-modified NPs (LNO-N₃, coating procedure detailed in the [Supporting Information](#) S-19) was ultrasonicated in the presence of complex 8, CuSO₄, and sodium ascorbate for 16 h, followed by repetitive cycles of centrifugation (10 min, 4700 rpm) and washings (H₂O, 3 times) to discard unreacted ligand and reagents ([Scheme 2](#)). The resulting conjugates (LNO-Gd) were suspended in distilled water (2 mg/mL) for further characterization. During the functionalization process, the mean hydrodynamic diameter of the HNPs increased from 61.9 ± 4.4 nm (bare LNO NPs) to 157 ± 4.7 nm (LNO-N₃) and 153 ± 11 nm (LNO-Gd), while the zeta potential value shifted from −39.03 ± 0.99 mV (bare LNO NPs) to 22.07 ± 0.09 mV (LNO-N₃) and −8.59 ± 0.33 mV (LNO-Gd).

Further analysis by scanning transmission electron microscopy (STEM) and energy-dispersive X-ray (EDX) spectroscopy is presented in [Figure 1A](#) (for a representative image of an ensemble of functionalized NPs, see [Supporting Information](#) Figure S2). The Si EDX map gave evidence for efficient silanization of the core NPs, which led to the formation of a dense coating layer averaging 10 nm thickness. A homogeneous distribution of the Gd(III)-containing complexes at the NP surface was confirmed in the Gd EDX map and merged elemental maps. The conjugation protocol resulted in up to 8 × 10⁴ chelates per NP (see [Supporting Information](#) S-22 for the calculation of the Gd(III) loading). XPS was used to probe and determine the Gd atomic concentration at the surface of LNO-Gd NPs, which was measured at 0.62% relative to the other surface elements ([Figure 1B](#); see the [Supporting Information](#), Figure S3 for survey and [Table S1](#) for the measured surface atomic concentrations). In addition, this

study revealed that traces of copper were efficiently removed from the samples of functionalized HNPs as the peak for Cu 2p could not be measured within the detection limit of the analysis.

Nonlinear Optical Imaging of LNO-Gd NPs. The nonlinear response of LNO NPs upon femtosecond pulse excitation was first reported at 800 nm (SHG)⁴⁹ and successively in the 700–1300 nm excitation range for SHG⁵⁰ and for other nonlinear and frequency mixing processes.⁵¹ Very recently, the SHG and THG from Mg-doped LNO NPs have been observed with excitation up to 2.2 μm .⁴² At 800 nm, the SHG efficiency of the LNO NPs studied here was determined from the ensemble measurements, leading to an orientation-averaged second-order susceptibility $\chi^{(2)}$ value of ~ 40 pm/V.⁵² In Figure 2, we present a complete set of multiphoton images obtained on DU145 human prostate cancer cells treated with LNO-Gd NPs at 50 $\mu\text{g/mL}$ following the protocol reported in the Experimental Section. The image series was selected to highlight (i) the emission tunability, (ii) the multiorder response, (iii) the narrow spectral-bandwidth of the harmonic signals, and (iv) the labeling properties of the nanoprobe presented in this work. Each panel label reports the excitation wavelength, along with the attribution of the signal (e.g., SHG @800 nm) and the spectral width of the corresponding detection channel. The SHG response is observed upon excitation at 800 and 1250 nm (i), SHG and THG are simultaneously detected upon 1250 nm excitation (ii), while under the same excitation, detection, and image plotting settings, barely any signal is visible within an adjacent nonoverlapping spectral range of the same width (iii). The DAPI channel allows identifying the cells present in the field of view. Although labeling is quite sparse, the NPs outline the morphology of most cells, displaying clearly their avoidance of the nuclear region (iv). We note that the labeling is not homogeneous for all cells: some of the cells in the left part of the image are labeled more faintly than the central ones.

Differently for the case of other materials,⁵³ we have not performed yet a thorough bioassessment of the interaction between LNO NPs and cells. Recently, Li et al. have studied the intracellular localization of LNO particles in mesenchymal stem cells within the size range used in our work and with a similar labeling protocol and particle concentration.⁵⁴ They reported that LNO NPs were internalized and accumulated preferentially in the perinuclear region and provided a concentration-dependent cytocompatibility assessment for this cell line.

Proton Relaxivity of the LNO-Gd NPs. To assess the ability of the LNO-Gd NPs to be used as MRI contrast agents, the longitudinal and transverse relaxation rates (R_1 and R_2 , respectively) of their monohydrated complex were measured at 60 MHz (1.4 T) at physiological temperature (37 $^{\circ}\text{C}$) (Table 1; see the Supporting Information for T_i values and additional measurements at 30 MHz, S-21). The calculated relaxivity values of **8** and LNO-Gd NPs, on a per millimolar Gd³⁺-ion basis, were compared to the characteristics reported for the ebpatcn-Gd chelate,⁴⁵ marketed Gd-chelates⁵⁵ (Magnevist, Multihance, r_1 measured at 1.5 T), and small polymer-coated gadolinium oxide NPs⁵⁶ (Dextran-SPGO, r_1 measured at 7.05 T). The r_2/r_1 ratio of the Gd(III)-chelate **8** is 1.1, which is consistent with the values reported for common low-molecular-weight Gd(III)-based T_1 contrast agents used in MRI bioimaging. The conjugation of this complex to the surface of LNO NPs led to a r_2/r_1 ratio of 2.4 for the resulting

Table 1. Relaxometric Characteristics of Complex **8, Functionalized LNO NPs (37 $^{\circ}\text{C}$, 1.4 T), and Marketed Gd-Chelate-Based Contrast Agents in Water**

	R_1 (s^{-1})	R_2 (s^{-1})	r_1 ($\text{mM}^{-1} \text{s}^{-1}$)	r_2 ($\text{mM}^{-1} \text{s}^{-1}$)
8	9.68	11.24	6.92	7.74
LNO NPs	0.26	0.63		
LNO-N ₃ NPs	0.29	0.89		
LNO-Gd NPs ^a	4.52	10.68	6.35	15
LNO-Gd NPs ^b			5.20×10^5	12.3×10^5
Gd(ebpatcn) (D ₂ O)			4.68 ^c	5.69 ^c
Magnevist			3.3 ^d	3.9 ^d
Multihance			4.0 ^d	4.3 ^d
dextran-SPGO (Gd ₂ O ₃ core)			4.8 ^e	16.9 ^e

^aRelaxivities calculated per Gd(III) chelate. ^bRelaxivities estimated per NP. ^cRelaxivities measured at 1.05 T and 25 $^{\circ}\text{C}$, from ref 45. ^dRelaxivities measured at 1.5 T, from ref 55. ^eRelaxivities measured at 7.05 T, from ref 56.

LNO-Gd NPs. Based on the Gd content, the relaxivity values r_1 , in the presence **8** or LNO-Gd NPs, are similar (6.92 and 6.35 $\text{mM}^{-1} \text{s}^{-1}$, respectively), indicating that the Gd(III) chelates at the NP surface adopt similar behavior as the species in solution. Such observation was previously disclosed on gold nanoconjugates⁵⁷ and multilayered assemblies of Gd(III) chelates on silica NPs.⁵⁸ Due to the high loading rate of chelate **8** to the NP surface, an estimated r_1 value of 5.20×10^5 $\text{mM}^{-1} \text{s}^{-1}$ was reached for the LNO-Gd NPs, on a per particle basis, which encouraged us to further evaluate their potential as contrast agents for T_1 -weighted MRI.

Evaluation of the LNO-Gd NPs as T_1 and T_2 Contrast Agents. Nowadays, most of the MRI scanners used for clinical diagnosis operate at high magnetic field strengths (>1.5 T),⁵⁹ in particular, those employed for whole-body human imaging applications. Therefore, the properties of the LNO-Gd NPs for contrast enhancement were investigated at 9.4 and 14.1 T. A commonly used agarose gel-based phantom^{60,61} was designed and composed of 11 NMR tubes (5 mm diameter) with different concentrations of LNO-Gd NPs (Table 2, Figure 3A). A single phantom experiment was performed using a 9.4 T NMR spectrometer to evaluate the T_1 spin–lattice and T_2 spin–spin relaxation times for increasing NP concentrations (0–1.5 mg/mL) (Figure 3B,C). A clear concentration-dependent enhancement of the R_1 relaxation rate and shortening of the T_1 relaxation time was observed over the studied concentration range, suggesting a signal-increasing imaging effect of the LNO-Gd NPs. The T_2 relaxation time also decreased as the LNO-Gd NP concentration increased, suggesting a decrease of the signal intensity as the concentration of the NPs increased.

The 2D T_1 - and T_2 -weighted images of the phantom were collected using a gradient-echo sequence/FLASH on a 14.1 T MRI system (Figure 4A,D), highlighting a concentration-dependent increase of the signal intensity for the T_1 -weighted images and a significant signal decrease for the T_2 -weighted images. In addition, quantitative T_1 mapping of the phantom demonstrated statistically significant ($p < 0.0001$) contrast enhancement correlated with LNO-Gd NP concentrations (Figure 4B,C), while the T_2 mapping revealed a statistically significant ($p < 0.0001$) contrast reduction (Figure 4E,F).

Most of the NP-based contrast agents used in clinics rely on superparamagnetic iron oxide (SPIO) materials which provide

Table 2. Composition of the Agarose Gel-Based Phantom

Sample	1	2	3	4	5	6	7	8	9	10	11
LNO-Gd NP concentration (mg/mL)	0.00	0.05	0.01	0.15	0.20	0.25	0.50	0.75	1.00	1.25	1.50

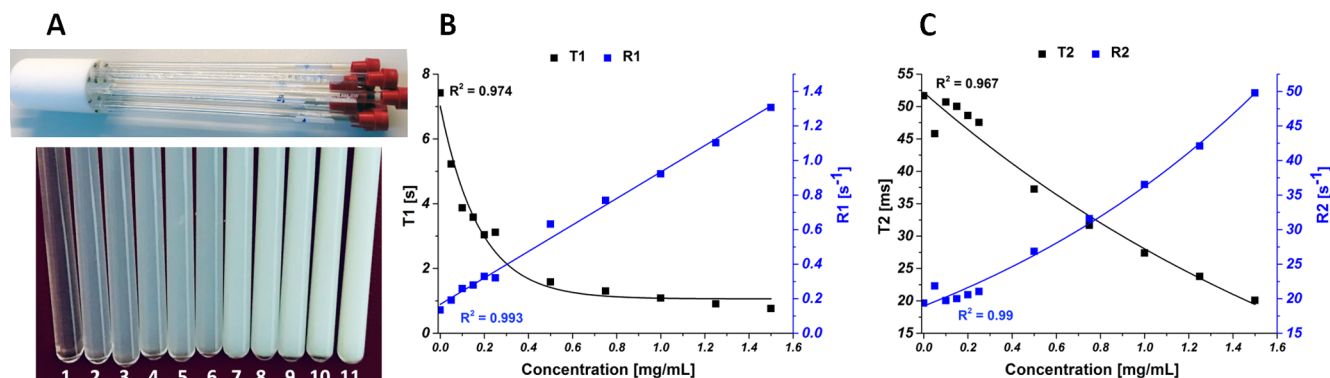


Figure 3. (A) Agarose gel-based phantom. (B) T_1 relaxation time and R_1 relaxation rate curves and (C) T_2 relaxation time and R_2 relaxation rate curves for LNO-Gd NP concentrations of 0–1.5 mg/mL at 9.4 T.

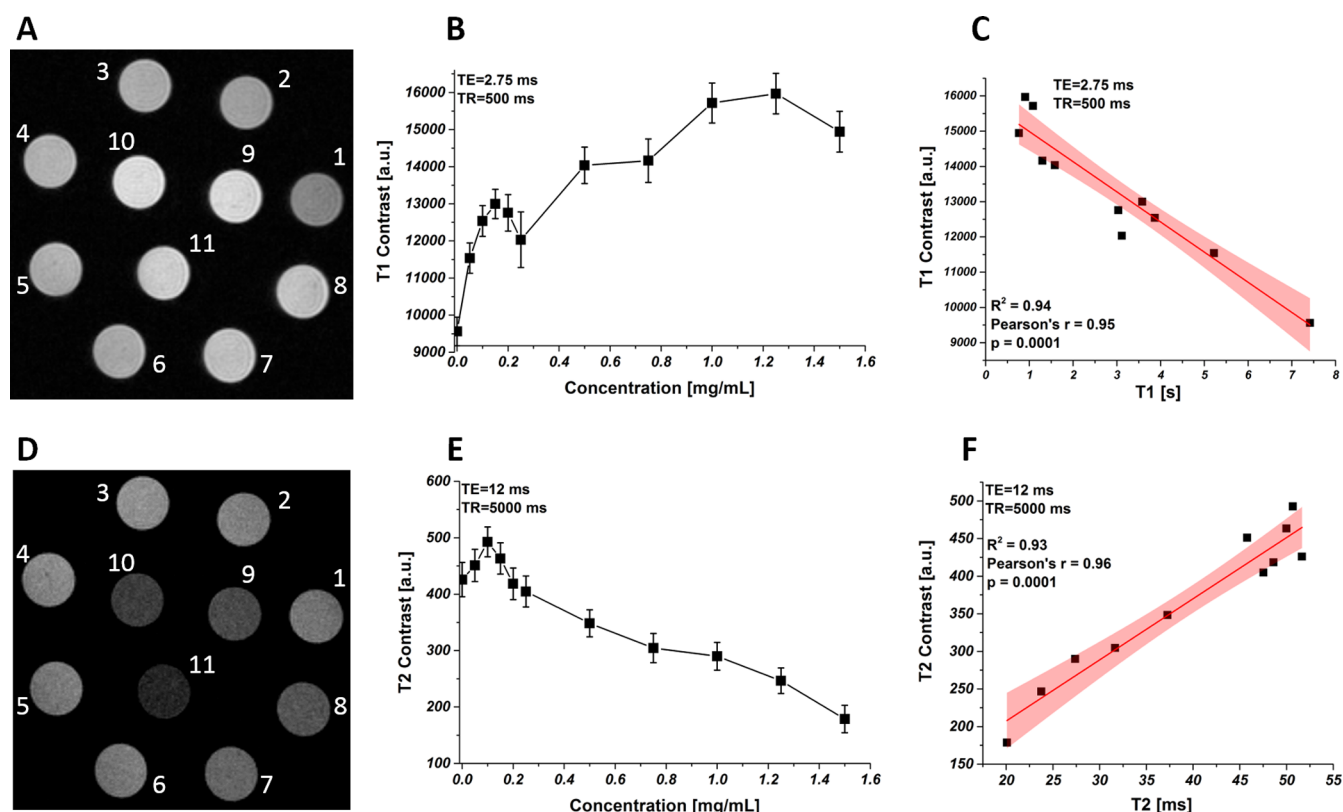


Figure 4. MR phantom images and contrast quantification at 14.1 T. (A) 2D T_1 -weighted and (D) 2D T_2 -weighted contrast image of the columnar phantom, FOV = 27.9×27.9 mm². (B,E) Contrast quantification curve. (C) Pearson correlation between the T_1 relaxation time and T_1 -weighted contrast enhancement and (F) Pearson correlation between T_2 relaxation time and T_2 -weighted contrast enhancement related to the LNO-Gd NP concentration increase.

a strong contrast enhancement in T_2 -weighted images, resulting in a signal-decreasing effect. Several limitations were reported for T_2 contrast agents, including the risk to confuse their dark signal with pathogenic lesions and their high susceptibility which is responsible for the distortion of the magnetic field on neighboring healthy tissues, so-called as the susceptibility artifact.⁶² Despite their strong capacity for positive contrast enhancement, T_1 contrast agents based on low-molecular-weight Gd(III) chelates suffer from short

circulation time *in vivo*, thus hampering MR image acquisition over long scan times. The development of NP-based contrast agents, combining T_1/T_2 dual-mode contrast efficiencies, appears as an appealing strategy to achieve the unequivocal detection of malignant lesions and improve the MRI diagnosis sensitivity.^{63,64} Recent reports disclosed the possibility of turning SPIO NPs into T_1/T_2 dual-mode contrast agents by the modulation of the size and shape of the metal oxide core.^{63,65} The combined loading of SPIO NPs and Fe³⁺ or

Gd³⁺ chelates^{66,67} into mesoporous nanomaterials showed high potential for the targeted T_1 – T_2 MRI of tumor tissues. The LNO-Gd nanoconjugates herein presented show a strong contrast enhancement in T_1 -weighted images, resulting from the homogeneous dispersion and high payload of Gd³⁺ chelates at their surface. Noteworthy, the comparison of the relaxivity values (r_1) at 1.4 T of the LNO-Gd NPs with commercial contrast agents suggests that excellent contrast should be obtained in short acquisition times on clinical MRI systems which generally operate at 3 and 7 T. Their capacity for contrast reduction in the T_2 imaging mode was also demonstrated. In addition, the labeling and efficient imaging of DU145 human prostate cancer cells was achieved by the same conjugates, thanks to the intense SHG signal of the inorganic core upon excitation at 810 nm. We also verified that the relaxometric properties of the LNO-Gd NPs remained unchanged after the excitation conditions applied for multiphoton imaging, indicating the stability of the surface conjugation to the Gd³⁺ chelates.

CONCLUSIONS

Surface-coated LNO HNPs conjugated to Gd(III) chelates represent appealing nanomaterials for the development of dual-imaging agents capable of exerting contrast both in MRI and nonlinear microscopy. A synthetic route was developed to prepare a lanthanide chelator based on the modification of the tripodal propionate ligand H₃ebpatcn with a terminal alkyne-containing homoserine derivative, allowing covalent conjugation to LNO-N₃ NPs using azide–alkyne [3 + 2]-cycloaddition. The substitution of the propionate group by a homoserine residue did not affect the coordination capacity of the ligand, as indicated by the results of relaxometric measurements on the Gd(III)-chelate **8**. A subsequent click reaction to coated HNPs led to LNO-Gd nanoconjugates presenting a homogeneous distribution of Gd(III)-containing complexes at the NP surface with a loading rate of up to 8×10^4 chelates per NP. The formation of a triazole moiety offers high stability of the Gd-functionalized HNPs in a physiological environment (pH variation and enzymatic cleavage). The LNO-Gd NPs exhibited strong concentration-dependent contrast enhancement in T_1 - and T_2 -weighted images of agarose gel-based phantoms, opening the prospects for dual-mode T_1/T_2 magnetic contrast formation, as well as intense multiharmonic signals for cancer cell imaging in the NIR windows. These combined properties highlight the potential of functionalized LNO HNPs to be used as imaging agents in complementary imaging techniques in terms of spatial resolution, penetration depth, and sensitivity. In addition to the previously established phototriggered drug delivery protocols^{47,68} and cell tracking capabilities^{37,38} of HNP-based conjugates, the dual imaging properties herein disclosed enlarge the scope of the LNO NPs toward theranostic applications.

ASSOCIATED CONTENT

Supporting Information

The Supporting Information is available free of charge at <https://pubs.acs.org/doi/10.1021/acsanm.2c00127>.

Additional results; synthesis protocols for compounds **5**; preparation of LNO-N₃ NPs; analytical data (¹H and ¹³C NMR spectra, IR data); TEM images of LNO NPs; surface atomic concentration of LNO-N₃ and LNO-Gd

NPs measured by XPS; and relaxometric properties of LNO, LNO-N₃, and LNO-Gd NPs (PDF)

AUTHOR INFORMATION

Corresponding Author

Sandrine Gerber-Lemaire – Institute of Chemical Sciences and Engineering, Ecole Polytechnique Fédérale de Lausanne, Group for Functionalized Biomaterials, EPFL SB ISIC SCI-SB-SG, CH-1015 Lausanne, Switzerland; orcid.org/0000-0002-6519-2782; Email: sandrine.gerber@epfl.ch

Authors

Raphaël De Matos – Institute of Chemical Sciences and Engineering, Ecole Polytechnique Fédérale de Lausanne, Group for Functionalized Biomaterials, EPFL SB ISIC SCI-SB-SG, CH-1015 Lausanne, Switzerland

Adrian Gheata – Institute of Chemical Sciences and Engineering, Ecole Polytechnique Fédérale de Lausanne, Group for Functionalized Biomaterials, EPFL SB ISIC SCI-SB-SG, CH-1015 Lausanne, Switzerland

Gabriel Campargue – Department of Applied Physics, Université de Genève, 1211 Genève 4, Switzerland

Jérémy Vuilleumier – Institute of Chemical Sciences and Engineering, Ecole Polytechnique Fédérale de Lausanne, Group for Functionalized Biomaterials, EPFL SB ISIC SCI-SB-SG, CH-1015 Lausanne, Switzerland

Laura Nicolle – Institute of Chemical Sciences and Engineering, Ecole Polytechnique Fédérale de Lausanne, Group for Functionalized Biomaterials, EPFL SB ISIC SCI-SB-SG, CH-1015 Lausanne, Switzerland

Katarzyna Pierzchala – Laboratory of Functional and Metabolic Imaging, Ecole Polytechnique Fédérale de Lausanne, CH-1015 Lausanne, Switzerland; Neurometabolic Unit, Service of Clinical Chemistry, University Hospital of Lausanne, CH-1015 Lausanne, Switzerland

Ileana Jelescu – Animal Imaging and Technology, Center for Biomedical Imaging, EPFL, CH-1015 Lausanne, Switzerland

Fiorella Lucarini – Faculty of Biology and Medicine, Department of Biomedical Sciences, Université de Lausanne, CH-1015 Lausanne, Switzerland

Ivan Gautschi – Faculty of Biology and Medicine, Department of Biomedical Sciences, Université de Lausanne, CH-1015 Lausanne, Switzerland

Florian Riporto – Université Savoie Mont-Blanc, SYMME, F-74000 Annecy, France

Ronan Le Dantec – Université Savoie Mont-Blanc, SYMME, F-74000 Annecy, France; orcid.org/0000-0002-6671-0879

Yannick Mugnier – Université Savoie Mont-Blanc, SYMME, F-74000 Annecy, France

Anne-Sophie Chauvin – Institute of Chemical Sciences and Engineering, Ecole Polytechnique Fédérale de Lausanne, Group of Coordination Chemistry, EPFL SB ISIC SCI-SB-MM, CH-1015 Lausanne, Switzerland; orcid.org/0000-0001-9222-3866

Marinella Mazzanti – Institute of Chemical Sciences and Engineering, Ecole Polytechnique Fédérale de Lausanne, Group of Coordination Chemistry, EPFL SB ISIC SCI-SB-MM, CH-1015 Lausanne, Switzerland; orcid.org/0000-0002-3427-008X

Davide Staedler – Animal Imaging and Technology, Center for Biomedical Imaging, EPFL, CH-1015 Lausanne, Switzerland

Dario Diviani – Animal Imaging and Technology, Center for Biomedical Imaging, EPFL, CH-1015 Lausanne, Switzerland
Luigi Bonacina – Department of Applied Physics, Université de Genève, 1211 Genève 4, Switzerland; orcid.org/0000-0003-0476-4473

Complete contact information is available at:
<https://pubs.acs.org/10.1021/acsanm.2c00127>

Author Contributions

The manuscript was written through contributions of all authors. R.D.M. designed and performed the functionalization pathways, prepared and characterized the hybrid NPs, and contributed to the relaxivity measurements. G.C. designed, performed, and analyzed the multiphoton imaging experiments. A.G. contributed to the preparation of the hybrid NPs and analyzed the HAADF-STEM images and EDX elemental maps. J.V. and L.N. contributed to the development of the synthetic and surface functionalization pathways. K.P. and I.J. prepared the phantom and performed the MRI experiments. F.R. prepared and characterized the bare LNO nanocrystals under the guidance of Y.M. and R.L.D. F.L., I.G., D.S., and D.D. contributed to the cell imaging experiments. A.S.C. and M.M. contributed to the design of the TACN-based chelating ligand. L.B. and S.G.L. supervised the project, designed the experiments, and prepared the manuscript. All authors have given approval to the final version of the manuscript.

Funding

This work was funded by the Interreg V Program (NANO-FIMT grant; OncoNanoScreen grant). The multiphoton imaging platform used for the optical measurements was funded by the Swiss National Foundation (R'Equip grant N° 316030-183529).

Notes

The authors declare no competing financial interest.

ACKNOWLEDGMENTS

The authors thank L. Menin (EPFL ISIC-MSEAP) for her support with MS characterizations, N. Gasilova (EPFL ISIC-MSEAP) for ICP-MS measurements, A. Bornet (EPFL ISIC-NMRP) for his assistance with relaxivity measurements, M. Mensi (EPFL ISIC-XRDSAP) for his support with XPS analyses, the Interdisciplinary Centre for Electron Microscopy (EPFL, CIME) for STEM experiments, S. Ghosh (UniGE, Department of Applied Physics) for her support with multiphoton image acquisition and processing, and S. Kaiser (UNIL, Faculty of Biology and Medicine, Department of Biomedical Sciences) for his support with cell labeling.

REFERENCES

(1) Forbes, S. J.; Rosenthal, N. Preparing the ground for tissue regeneration: from mechanism to therapy. *Nat. Med.* **2014**, *20*, 857–869.
(2) Waldman, A. D.; Fritz, J. M.; Lenardo, M. J. A guide to cancer immunotherapy: from T cell basic science to clinical practice. *Nat. Rev. Immunol.* **2020**, *20*, 651–668.
(3) Kircher, M. F.; Gambhir, S. S.; Grimm, J. Noninvasive cell-tracking methods. *Nat. Rev. Clin. Oncol.* **2011**, *8*, 677–688.
(4) Ni, J.-S.; Li, Y.; Yue, W.; Liu, B.; Li, K. Nanoparticle-based Cell Trackers for Biomedical Applications. *Theranostics* **2020**, *10*, 1923–1947.
(5) Kim, J.; Chhour, P.; Hsu, J.; Litt, H. I.; Ferrari, V. A.; Popovtzer, R.; Cormode, D. P. Use of Nanoparticle Contrast Agents for Cell

Tracking with Computed Tomography. *Bioconjugate Chem.* **2017**, *28*, 1581–1597.
(6) Sordillo, L. A.; Pu, Y.; Pratavieira, S.; Budansky, Y.; Alfano, R. R. Deep optical imaging of tissue using the second and third near-infrared spectral windows. *J. Biomed. Opt.* **2014**, *19*, 056004.
(7) Kobat, D.; Durst, M. E.; Nishimura, N.; Wong, A. W.; Schaffer, C. B.; Xu, C. Deep Tissue Multiphoton Microscopy Using Longer Wavelength Excitation. *Opt. Express* **2009**, *17*, 13354–13364.
(8) Bruns, O. T.; Bischof, T. S.; Harris, D. K.; Franke, D.; Shi, Y.; Riedemann, L.; Jaworski, F. B.; Carr, J. A.; Rowlands, C. J.; Wilson, M. W. B.; Chen, O.; Wie, H.; Hwang, G. W.; Montana, D. M.; Coropceanu, I.; Achorn, O. B.; Kloepper, J.; Heeren, J.; So, P. T. C.; Fukumura, D.; Jensen, K. F.; Jain, R. K.; Bawendi, M. G. Next-Generation In Vivo Optical Imaging with Short-Wave Infrared Quantum Dots. *Nat. Biomed. Eng.* **2017**, *1*, 1–11.
(9) Naczynski, D.; Tan, M.; Zevon, M.; Wall, B.; Kohl, J.; Kulesa, A.; Chen, S.; Roth, C. M.; Riman, R. E.; Moghe, P. V. Rare-earth-doped biological composites as in vivo shortwave infrared reporters. *Nat. Commun.* **2013**, *4*, 2199.
(10) Ali, Z.; Abbasi, A. Z.; Zhang, F.; Arosio, P.; Lascialfari, A.; Casula, M. F.; Wenk, A.; Kreyling, W.; Plapper, R.; Seidel, M.; Niessner, R.; Knöll, J.; Seubert, A.; Parak, W. J. Multifunctional Nanoparticles for Dual Imaging. *Anal. Chem.* **2011**, *83*, 2877–2882.
(11) Chen, H.; Zhang, W.; Zhu, G.; Xie, J.; Chen, X. Rethinking Cancer Nanotheranostics. *Nat. Rev. Mater.* **2017**, *2*, 17024.
(12) Stafford, S.; Serrano Garcia, R.; Gun'ko, Y. Multimodal Magnetic-Plasmonic Nanoparticles for Biomedical Applications. *Appl. Sci.* **2018**, *8*, 97.
(13) Liu, T.-M.; Conde, J.; Lipiński, T.; Bednarkiewicz, A.; Huang, C.-C. Smart NIR Linear and Nonlinear Optical Nanomaterials for Cancer Theranostics: Prospects in Photomedicine. *Prog. Mater. Sci.* **2017**, *88*, 89–135.
(14) Liu, M.; Anderson, R.-C.; Lan, X.; Conti, P. S.; Chen, K. Recent Advances in the Development of Nanoparticles for Multimodality Imaging and Therapy of Cancer. *Med. Res. Rev.* **2019**, *40*, 909.
(15) Xu, J.; Gulzar, A.; Yang, D.; Gai, S.; He, F.; Yang, P. Tumor Self-Responsive Upconversion Nanomedicines for Theranostic Applications. *Nanoscale* **2019**, *11*, 17535–17556.
(16) Du, Z.; Gupta, A.; Clarke, C.; Cappadona, M.; Clases, D.; Liu, D.; Yang, Z.; Karan, S.; Price, W. S.; Xu, X. Porous Upconversion Nanostructures as Bimodal Biomedical Imaging Contrast Agents. *J. Phys. Chem. C* **2020**, *124*, 12168–12174.
(17) Norouzi, M. Gold Nanoparticles in Glioma Theranostics. *Pharmacol. Res.* **2020**, *156*, 104753.
(18) Sun, Y.; Yu, M.; Liang, S.; Zhang, Y.; Li, C.; Mou, T.; Yang, W.; Zhang, X.; Li, B.; Huang, C.; Li, F. Fluorine-18 Labeled Rare-Earth Nanoparticles for Positron Emission Tomography (PET) Imaging of Sentinel Lymph Node. *Biomaterials* **2011**, *32*, 2999–3007.
(19) Zhou, J.; Yu, M.; Sun, Y.; Zhang, X.; Zhu, X.; Wu, D.; Li, F. Fluorine-18-Labeled Gd³⁺/Yb³⁺/Er³⁺ Co-Doped NaYF₄ nanophosphors for multimodality PET/MR/UCL imaging. *Biomaterials* **2011**, *32*, 1148–1156.
(20) Ilves, V. G.; Sokovnin, S. Y.; Zuev, M. G.; Uimin, M. A.; Privalova, D. V.; Kozlova, J.; Sammelsetg, V. Multimodal Upconversion CaF₂:Mn/Yr/Er/Si Nanoparticles. *J. Fluorine Chem.* **2020**, *231*, 109457.
(21) Li, H.; Wang, X.; Huang, D.; Chen, G. Recent Advances of Lanthanide-Doped Upconversion Nanoparticles for Biological Applications. *Nanotechnology* **2020**, *31*, 072001.
(22) Sun, Y.; Zhu, X.; Peng, J.; Li, F. Core-Shell Lanthanide Upconversion Nanophosphors as Four-Modal Probes for Tumor Angiogenesis Imaging. *ACS Nano* **2013**, *7*, 11290–11300.
(23) Lee, H.-Y.; Li, Z.; Chen, K.; Hsu, A. R.; Xu, C.; Xie, J.; Sun, S.; Chen, X. PET/MRI Dual-Modality Tumor Imaging Using Arginine-Glycine-Aspartic (RGD)-Conjugated Radiolabeled Iron Oxide Nanoparticles. *J. Nucl. Med.* **2008**, *49*, 1371–1379.
(24) Pillariseti, S.; Uthaman, S.; Huh, K. M.; Koh, Y. S.; Lee, S.; Park, I.-K. Multimodal Composite Iron Oxide Nanoparticles for

Biomedical Applications. *Tissue Eng. Regen. Med.* **2019**, *16*, 451–465.

(25) Hu, D.-H.; Sheng, Z.-H.; Zhang, P.-F.; Yang, D.-Z.; Liu, S.-H.; Gong, P.; Gao, D.-Y.; Fang, S.-T.; Ma, Y.-F.; Cai, L.-T. Hybrid Gold-Gadolinium Nanoclusters for Tumor-Targeted NIRF/CT/MRI Triple-Modal Imaging In Vivo. *Nanoscale* **2013**, *5*, 1624–1328.

(26) Xu, C.; Wang, Y.; Zhang, C.; Jia, Y.; Luo, Y.; Gao, X. AuGd Integrated Nanoprobes for Optical/MRI/CT triple-modal in vivo tumor targeting. *Nanoscale* **2017**, *9*, 4620–4628.

(27) Stasiuk, G. J.; Tamang, S.; Imbert, D.; Poillot, C.; Giardiello, M.; Tisseyre, C.; Barbier, E. L.; Fries, P. H.; de Waard, M.; Reiss, P.; Mazzanti, M. Cell-Permeable Ln(III) Chelate-Functionalized InP Quantum Dots as Multimodal Imaging Agents. *ACS Nano* **2011**, *5*, 8193–8201.

(28) Wartenberg, N.; Fries, P.; Raccurt, O.; Guillermo, A.; Imbert, D.; Mazzanti, M. A Gadolinium Complex Confined in Silica Nanoparticles as a Highly Efficient T₁/T₂ MRI Contrast Agent. *Chem.—Eur. J.* **2013**, *19*, 6980–6983.

(29) Kim, J. S.; Rieter, W. J.; Taylor, K. M. L.; An, H.; Lin, W.; Lin, W. Self-Assembled Hybrid Nanoparticles for Cancer-Specific Multimodal Imaging. *J. Am. Chem. Soc.* **2007**, *129*, 8962–8963.

(30) Albuquerque, G. M.; Souza-Sobrinha, I.; Coiado, S. D.; Santos, B. S.; Fontes, A.; Pereira, G. A. L.; Pereira, G. Quantum Dots and Gd³⁺ Chelates: Advances and Challenges Toward Bimodal Nanoprobes for Magnetic Resonance and Optical Imaging. *Top. Curr. Chem.* **2021**, *379*, 12.

(31) Debroye, E.; Parac-Vogt, T. N. Towards Polymetallic Lanthanide Complexes as Dual Contrast Agents for Magnetic Resonance and Optical Imaging. *Chem. Soc. Rev.* **2014**, *43*, 8178–8192.

(32) Dempsey, W. P.; Fraser, S. E.; Pantazis, P. SHG Nanoprobes: Advancing Harmonic Imaging in Biology. *BioEssays* **2012**, *34*, 351–360.

(33) Bonacina, L. Nonlinear Nanomedicine: Harmonic Nanoparticles toward Targeted Diagnosis and Therapy. *Mol. Pharmaceutics* **2013**, *7*, 205–209.

(34) Grange, R.; Lanvin, T.; Hsieh, C.-L.; Pu, Y.; Psaltis, D. Imaging with Second-Harmonic Radiation Probes in Living Tissue. *Biomed. Opt. Express* **2011**, *2*, 2532–2539.

(35) Le Xuan, L.; Zhou, C.; Slablab, A.; Chauvat, D.; Tard, C.; Perruchas, S.; Gacoin, T.; Villeval, P.; Roch, J.-F. Photostable Second-Harmonic Generation from a Single KTiOPO₄ Nanocrystal for Nonlinear Microscopy. *Small* **2008**, *4*, 1332–1336.

(36) Rogov, A.; Irondele, M.; Ramos Gomes, F.; Bode, J.; Staedler, D.; Passemard, S.; Courvoisier, S.; Yamamoto, Y.; Waharte, F.; Ciepielewski, D.; Rideau, P.; Gerber-Lemaire, S.; Alves, F.; Salamero, J.; Bonacina, L.; Wolf, J.-P. Simultaneous Multi-Harmonic Imaging of Nanoparticles in Tissues for Increased Selectivity. *ACS Photonics* **2015**, *2*, 1416–1422.

(37) Dubreil, L.; Leroux, I.; Ledevin, M.; Schleder, C.; Lagalice, L.; Lovo, C.; Fleurisson, R.; Passemard, S.; Kilin, V.; Gerber-Lemaire, S.; Colle, M.-A.; Bonacina, L.; Rouger, K. Multi-Harmonic Imaging in the Second Near-Infrared Window of Nanoparticle-Labeled Stem Cells as Effective Monitoring Tool in Tissue Depth. *ACS Nano* **2017**, *11*, 6672–6681.

(38) Ramos-Gomes, F.; Möbius, W.; Bonacina, L.; Alves, F.; Markus, M. A. Bismuth Ferrite Second Harmonic Nanoparticles for Pulmonary Macrophage Tracking. *Small* **2019**, *15*, No. e1803776.

(39) Sugiyama, N.; Sonay, A. Y.; Tussiwand, R.; Cohen, B. E.; Pantazis, P. Effective Labeling of Primary Somatic Stem Cells with BaTiO₃ Nanocrystals for Second Harmonic Generation Imaging. *Small* **2018**, *14*, 1703386.

(40) Čulić-Viskotski, J.; Dempsey, W. P.; Fraser, S. E.; Pantazis, P. Surface Functionalization of Barium Titanate SHG Nanoprobes for In Vivo Imaging in Zebrafish. *Nat. Protoc.* **2012**, *7*, 1618–1633.

(41) Vittadello, L.; Kijatkin, C.; Klenen, J.; Dzikowski, D.; Kömpe, K.; Meyer, C.; Paululat, A.; Imlau, M. In-Vivo Tracking of Harmonic Nanoparticles: a Study Based on a TIGER Widefield Microscope. *Opt. Mater. Express* **2021**, *11*, 1953–1969.

(42) Vittadello, L.; Klenen, J.; Koempe, K.; Kocsor, L.; Szaller, Z.; Imlau, M. NIR-to-NIR Imaging: Extended Excitation Up to 2.2 μm Using Harmonic Nanoparticles with a Tunable hGH EneRgy (TIGER) Widefield Microscope. *Nanomaterials* **2021**, *11*, 3193.

(43) Madzharova, F.; Nodar, A.; Živanović, V.; Huang, M. R. S.; Koch, C. T.; Esteban, R.; Aizpurua, J.; Kneipp, J. Gold- and Silver-Coated Barium Titanate Nanocomposites as Probes for Two-Photon Multimodal Microspectroscopy. *Adv. Funct. Mater.* **2019**, *29*, 1904289.

(44) Urbain, M.; Riporto, F.; Beauquis, S.; Monnier, V.; Marty, J.-C.; Galez, C.; Durand, C.; Chevolot, Y.; Dantec, R. L.; Mugnier, Y. On the Reaction Pathways and Growth Mechanisms of LiNbO₃ Nanocrystals from the Non-Aqueous Solvothermal Alkoxide Route. *Nanomaterials* **2021**, *11*, 154.

(45) Nonat, A.; Giraud, M.; Gateau, C.; Fries, P. H.; Helm, L.; Mazzanti, M. Gadolinium(III) Complexes of 1,4,7-Triazacyclononane Based Picolinate Ligands: Simultaneous Optimization of Water Exchange Kinetics and Electronic Relaxation. *Dalton Trans.* **2009**, *38*, 8033–8046.

(46) De Matos, R. J. Surface Functionalization of Metal Oxide Harmonic Nanoparticles for Targeted Cancer Imaging. Doctoral Dissertation, Ecole Polytechnique Fédérale de Lausanne, Lausanne, 2020.

(47) Vuilleumier, J.; Gaulier, G.; De Matos, R.; Ortiz, D.; Menin, L.; Campargue, G.; Mas, C.; Constant, S.; Le Dantec, R.; Mugnier, Y.; Bonacina, L.; Gerber-Lemaire, S. Two-Photon-Triggered Photo-release of Caged Compounds from Multifunctional Harmonic Nanoparticles. *ACS Appl. Mater. Interfaces* **2019**, *11*, 27443–27452.

(48) Nonat, A.; Gateau, C.; Fries, P. H.; Mazzanti, M. Lanthanide Complexes of a Picolinate Ligand Derived from 1,4,7-Triazacyclononane with Potential Application in Magnetic Resonance Imaging and Time-Resolved Luminescence Imaging. *Chem.—Eur. J.* **2006**, *12*, 7133–7150.

(49) Staedler, D.; Magouroux, T.; Hadji, R.; Joulaud, C.; Extermann, J.; Schwung, S.; Passemard, S.; Kasparian, C.; Clarke, G.; Gerrmann, M.; Le Dantec, R.; Mugnier, Y.; Rytz, D.; Ciepielewski, D.; Galez, C.; Gerber-Lemaire, S.; Juillerat-Jeanneret, L.; Bonacina, L.; Wolf, J.-P. Harmonic Nanocrystals for Biolabeling: a Survey of Optical Properties and Biocompatibility. *ACS Nano* **2012**, *6*, 2542–2549.

(50) Timpu, F.; Sendra, J.; Renaut, C.; Lang, L.; Timofeeva, M.; Buscaglia, M. T.; Buscaglia, V.; Grange, R. Lithium Niobate Nanocubes as Linear and Nonlinear Ultraviolet Mie Resonators. *ACS Photonics* **2019**, *6*, 545–552.

(51) Campargue, G.; La Volpe, L.; Giardina, G.; Gaulier, G.; Lucarini, F.; Gautschi, I.; Le Dantec, R.; Staedler, D.; Diviani, D.; Mugnier, Y.; Wolf, J.-P.; Bonacina, L. Multiorder Nonlinear Mixing in Metal Oxide Nanoparticles. *Nano Lett.* **2020**, *20*, 8725–8732.

(52) Riporto, J.; Urbain, M.; Mugnier, Y.; Multian, V.; Riporto, F.; Bredillet, K.; Beauquis, S.; Galez, C.; Monnier, V.; Chevolot, Y.; Gayvoronsky, V.; Bonacina, L.; Le Dantec, R. Second Harmonic Spectroscopy of ZnO, BiFeO₃ and LiNbO₃ Nanocrystals. *Opt. Mater. Express* **2019**, *9*, 1955–1966.

(53) Staedler, D.; Passemard, S.; Magouroux, T.; Rogov, A.; Maguire, C. M.; Mohamed, B. M.; Schwung, S.; Rytz, D.; Jüstel, T.; Hwu, S.; Mugnier, Y.; Le Dantec, R.; Volkov, Y.; Gerber-Lemaire, S.; Prina-Mello, A.; Bonacina, L.; Wolf, J.-P. Cellular Uptake and Biocompatibility of Bismuth Ferrite Harmonic Advanced Nanoparticles. *Nanomedicine: NBM* **2015**, *11*, 815–824.

(54) Li, J.; Qiu, J.; Guo, W.; Wang, S.; Ma, B.; Mou, X.; Tanes, M.; Jiang, H.; Liu, H. Cellular Internalization of LiNbO₃ Nanocrystals for Second Harmonic Imaging and the Effects on Stem Cell Differentiation. *Nanoscale* **2016**, *8*, 7416–7422.

(55) Rohrer, M.; Bauer, H.; Mintonovitch, J.; Requardt, M.; Weinmann, H.-J. Comparison of Magnetic Properties of MRI Contrast Media Solutions at Different Magnetic Field Strengths. *Invest. Radiol.* **2005**, *40*, 715–724.

(56) McDonald, M. A.; Watkin, K. L. Investigations into the Physicochemical Properties of Dextran Small Particulate Gadolinium Oxide Nanoparticles. *Acad. Radiol.* **2006**, *13*, 421–427.

(57) Debouttière, P.-J.; Roux, S.; Vocanson, F.; Billotey, C.; Beuf, O.; Favre-Réguillon, A.; Lin, Y.; Pellet-Rostaing, S.; Lamartine, R.; Perriat, P.; Tillement, O. Design of Gold Nanoparticles for Magnetic Resonance Imaging. *Adv. Funct. Mater.* **2006**, *16*, 2330–2339.

(58) Rieter, W. J.; Kim, J. S.; Taylor, K. M. L.; An, H.; Lin, W.; Tarrant, T.; Lin, W. Hybrid Silica Nanoparticles for Multimodal Imaging. *Angew. Chem., Int. Ed.* **2007**, *46*, 3680–3682.

(59) Tunariu, N.; Blackledge, M.; Messiou, C.; Petralia, G.; Padhani, A.; Curcean, S.; Curcean, A.; Koh, D.-M. What's New for Clinical Whole-Body MRI (WB-MRI) in the 21st Century. *Br. J. Radiol.* **2020**, *93*, 20200562.

(60) Mitchell, M. D.; Kundel, H. L.; Axel, L.; Joseph, P. M. Agarose as a Tissue Equivalent Phantom Materials for NMR imaging. *Magn. Reson. Imaging* **1986**, *4*, 263–266.

(61) Hellerbach, A.; Schuster, V.; Jansen, A.; Sommer, J. MRI Phantoms—Are There Alternatives to Agar? *PLoS One* **2013**, *8*, No. e70343.

(62) Na, H. B.; Song, I. C.; Hyeon, T. Inorganic Nanoparticles for MRI Contrast Agents. *Adv. Mater.* **2009**, *21*, 2133–2148.

(63) Alipour, A.; Soran-Erdem, Z.; Utkur, M.; Sharma, V. K.; Algin, O.; Saritas, E. U.; Demir, H. V. A New Class of Cubic SPIONs as a Dual-Mode T₁ and T₂ Contrast Agent for MRI. *Magn. Reson. Imaging* **2018**, *49*, 16–24.

(64) Liu, D.; Li, J.; Wang, C.; An, L.; Lin, J.; Tian, Q.; Yang, S. Ultrasmall Fe@Fe₃O₄ Nanoparticles as T₁-T₂ Dual-Mode MRI Contrast Agents for Targeted Tumor Imaging. *Nanomedicine: NBM* **2021**, *32*, 102335.

(65) Sánchez-Cabezas, S.; Montes-Robles, R.; Gallo, J.; Sancenón, F.; Martínez-Mañez, R. Combining Magnetic Hyperthermia and Dual T₁/T₂ MR Imaging Using Highly Versatile Iron Oxide Nanoparticles. *Dalton Trans.* **2019**, *48*, 3883–3892.

(66) Shu, G.; Chen, M.; Song, J.; Xu, X.; Lu, C.; Du, Y.; Xu, M.; Zhao, Z.; Zhu, M.; Fan, K.; Fan, X.; Fang, S.; Tang, B.; Dai, Y.; Du, Y.; Ji, J. Sialic Acid-Engineered Mesoporous Polydopamine Nanoparticles Loaded with SPIO and Fe³⁺ as a Novel Theranostic Agent for T₁/T₂ Dual-Mode MRI-Guided Combined Chemo-Photothermal Treatment of Hepatic Cancer. *Bioact. Mater.* **2021**, *6*, 1423–1435.

(67) Gao, L.; Yu, J.; Liu, Y.; Zhou, J.; Sun, L.; Wang, J.; Zhu, J.; Peng, H.; Lu, W.; Yu, L.; Yan, Z.; Wang, Y. Tumor-Penetrating Peptide Conjugated and Doxorubicin Loaded T₁-T₂ Dual Mode MRI Contrast Agents Nanoparticles for Tumor Theranostics. *Theranostics* **2018**, *8*, 92–108.

(68) Vuilleumier, J.; Gaulier, G.; De Matos, R.; Mugnier, Y.; Campargue, G.; Wolf, J.-P.; Bonacina, L.; Gerber-Lemaire, S. Photocontrolled Release of the Anticancer Drug Chlorambucil with Caged Harmonic Nanoparticles. *Helv. Chim. Acta* **2020**, *103*, No. e1900251.

Recommended by ACS

Unimolecular Nano-contrast Agent with Ultrahigh Relaxivity and Very Long Retention for Magnetic Resonance Lymphography

Lu Xu, Yongming Chen, *et al.*

MAY 13, 2022
NANO LETTERS

READ 

Cerium Oxide Nanoparticles with Entrapped Gadolinium for High T₁ Relaxivity and ROS-Scavenging Purposes

Peter Eriksson, Kajsa Uvdal, *et al.*

JUNE 07, 2022
ACS OMEGA

READ 

High Relaxivity with No Coordinated Waters: A Seemingly Paradoxical Behavior of [Gd(DOTP)]⁵⁻ Embedded in Nanogels

Fabio Carniato, Mauro Botta, *et al.*

MARCH 22, 2022
INORGANIC CHEMISTRY

READ 

Near-Infrared Emitting Poly(amidoamine) Dendrimers with an Anthraquinone Core toward Versatile Non-Invasive Biological Imaging

Kamal Jouad, Franck Suzenet, *et al.*

MARCH 02, 2022
BIOMACROMOLECULES

READ 

Get More Suggestions >